

## References and Notes

- Y. Ueno, Y. Isozaki, H. Yurimoto, S. Maruyama, *Int. Geol. Rev.* **43**, 196 (2001).
- S. M. Awramik, J. W. Schopf, M. R. Walter, *Precambrian Res.* **20**, 357 (1983).
- J. W. Schopf, M. R. Walter, in *Earth's Earliest Biosphere*, J. W. Schopf, Ed. (Princeton Univ. Press, Princeton, NJ, 1983), chap. 9.
- J. W. Schopf, B. M. Packer, *Science* **237**, 70 (1987).
- J. W. Schopf, *Science* **260**, 640 (1993).
- J. W. Schopf, A. B. Kudryavtsev, D. G. Agresti, T. J. Wdowiak, A. D. Czaja, *Nature* **416**, 73 (2002).
- J. D. Pasteris, B. Wopenka, *Nature* **420**, 476 (2002).
- I. L. Svensson, S. Sjöberg, L.-O. Öhman, *J. Chem. Soc. Faraday Trans. 1* **82**, 3635 (1986).
- R. M. Garrels, C. L. Christ, *Solutions, Minerals and Equilibria* (Harper & Row, New York, 1965).
- T. Baird et al., *Mater. Res. Bull.* **27**, 1031 (1992).
- J. M. García-Ruiz, A. Moreno, *Anales Quimica Int. Ed.* **93**, 1 (1997).
- J. M. García-Ruiz, A. Carnerup, A. G. Christy, N. J. Welham, S. T. Hyde, *Astrobiology* **2**, 335 (2002).
- Available as supporting material on Science Online.
- P. G. De Gennes, J. Prost, *The Physics of Liquid Crystals* (Clarendon, Oxford, 1993).
- J. H. E. Cartwright, J. M. García-Ruiz, M. L. Novella, F. Otarola, *J. Colloid Interface Sci.* **256**, 351 (2002).
- H. A. Lowenstam, S. Weiner, *On Biomineralization* (Oxford Univ. Press, Oxford, 1989).
- R. Buick, *Palaio* **5**, 441 (1990).
- B. A. Hofmann, J. D. Farmer, *Planet. Space Sci.* **48**, 1077 (2000).
- M. D. Brasier et al., *Nature* **416**, 76 (2002).
- P. E. Cloud, K. Morrison, *Precambrian Res.* **9**, 81 (1979).
- T.-H. Ko, W.-S. Kuo, Y.-H. Chang, *Polym. Compos.* **21**, 745 (2000).
- J. M. García-Ruiz, in *Carbonate Sedimentation and Diagenesis in the Evolving Precambrian World*, J. P. Grotzinger, N. P. James, Eds. (SEPM Special Publication 67, Society for Sedimentary Geology, Tulsa, OK, 2000), pp. 75–89.
- J. M. García-Ruiz, *Geology* **26**, 843 (1998).
- R. I. Thorpe, A. H. Hickman, D. W. Davis, J. K. Mortensen, A. F. Trendall, in *The Archaean: Terrains, Processes and Metallogeny*, J. E. Glover, S. Ho, Eds. (Geology Department and University Extension, The University of Western Australia, 1992), pp. 395–408.
- M. J. Van Kranendonk, in preparation.
- T. M. McCollom, *Geochim. Cosmochim. Acta* **67**, 311 (2003).
- J. M. Hunt, M. D. Lewan, R. J.-C. Hennet, *Am. Assoc. Petrol. Geol. Bull.* **75**, 795 (1991).
- D. A. Wood, *Am. Assoc. Petrol. Geol. Bull.* **72**, 115 (1988).
- H. Yang, N. Coombs, G. A. Ozin, *Nature* **386**, 692 (1997).
- We thank J. Doherty [formerly Applied Maths, Australian National University (ANU); now at Australian Capital Territory Government Analytical Laboratory] for her research contributions; also F. Brink, C. Huang, and S. Stowe of the Electron Microscopy Unit, ANU; U. Troitzsch (Department of Geology, ANU); and V. Otieno-Alego (formerly Corrosion and Spectrochemistry Laboratory, University of Canberra; now Australian Federal Police Forensic Laboratory) for their assistance and advice. Published with permission of the director of the Geological Survey of Western Australia.

## Supporting Online Material

www.sciencemag.org/cgi/content/full/302/5648/1194/DC1

Materials and Methods

Figs. S1 to S3

Movies S1 to S4

Table S1

6 August 2003; accepted 6 October 2003

## Intraslab Earthquakes: Dehydration of the Cascadia Slab

Leiph A. Preston,<sup>1\*</sup> Kenneth C. Creager,<sup>1</sup> Robert S. Crosson,<sup>1</sup> Thomas M. Brocher,<sup>2</sup> Anne M. Trehu<sup>3</sup>

We simultaneously invert travel times of refracted and wide-angle reflected waves for three-dimensional compressional-wave velocity structure, earthquake locations, and reflector geometry in northwest Washington state. The reflector, interpreted to be the crust-mantle boundary (Moho) of the subducting Juan de Fuca plate, separates intraslab earthquakes into two groups, permitting a new understanding of the origins of intraslab earthquakes in Cascadia. Earthquakes up-dip of the Moho's 45-kilometer depth contour occur below the reflector, in the subducted oceanic mantle, consistent with serpentinite dehydration; earthquakes located down-dip occur primarily within the subducted crust, consistent with the basalt-to-eclogite transformation.

The most damaging earthquakes in western Washington have been intraslab events, also known as Wadati-Benioff earthquakes. These include earthquakes in 1949, 1965, and, most recently, the 2001 moment magnitude ( $M_w$ ) 6.8 Nisqually event. Although megathrust earthquakes are typically larger in magnitude, intraslab events can be more damaging because they often occur directly beneath population centers, may have shorter recurrence intervals (as in Washington), and tend to have larger seismic energy-to-moment ratios ( $I$ ) than megathrust events have.

The physical mechanisms responsible for intraslab earthquakes in the depth range 30 to 200 km have been debated for de-

cadecades. A prominent theory, dehydration embrittlement, asserts that volatiles released during metamorphic dehydration reactions reduce the effective normal stresses across faults, allowing slip (2, 3). In light of the damaging 2001 Nisqually ( $M_w$  6.8), 2001 Geiyo, Japan ( $M_w$  6.7), and 2001 El Salvador ( $M_w$  7.7) intraslab earthquakes, gaining physical insight into the mechanics controlling these earthquakes is important for earthquake hazard estimates and mitigation efforts. The 1998 Seismic Hazards Investigation in Puget Sound (Wet SHIPS) experiment (4) provided an opportunity to investigate the high-resolution structure of the subducting plate in northwest Washington and southwest British Columbia (5).

The Juan de Fuca plate is relatively young and warm (maximum age ~10 million years), subducting obliquely at about 40 mm/year northeastward under Washington and Oregon. Active intraslab seismicity extends to 60-km depth, with some small events reaching depths as great as 100 km (6).

The data for the structural inversion consist of 90,000 first-arrival travel times from the Wet SHIPS, Dry SHIPS, western Cascades, and southwest Washington experiments (fig. S1) (7, 8); 27,000 first-arrival times from 1400 local earthquakes [200 of which are intraslab events (9)]; and 1200 secondary arrivals from the Wet SHIPS experiment that are consistent in slowness and travel time with reflections from the Juan de Fuca slab. We developed a nonlinear iterative inversion scheme that simultaneously inverts these travel times for earthquake locations, three-dimensional (3D) velocity structure, and reflector geometry (10). A well-known trade-off exists between reflector depth and velocity structure. By including independent first-arrival information, we reduce this trade-off and extract reliable reflector depths. A smooth velocity model is regularized by minimizing second-order spatial derivatives of the velocity structure and reflector surface. Travel times of first arrivals are calculated using the Vidale-Hole (11, 12) 3D finite-difference code. Theoretical reflected bounce points and travel times are determined by summing calculated travel times from the source and receiver to points on the reflector surface and determining the position and time corresponding to the minimum summed time according to Fermat's principle. Reflected rays are then independently traced from the bounce point to the source and to the receiver. Reflector geometry and the 3D velocity model are each adjusted to fit the times of reflected waves. This nonlinear procedure converges stably after 10 iterations. The final model gives root mean square travel-time residuals of 0.09, 0.12, and 0.08 s for the active-source, earthquake, and reflection data, respectively, amounting to variance reductions of 98 and 91% for the active-source and earthquake travel times, respectively, relative to the standard regional 1D velocity model (13).

<sup>1</sup>Department of Earth and Space Sciences, University of Washington, Seattle, WA 98195, USA. <sup>2</sup>U.S. Geological Survey, Menlo Park, CA 94025, USA. <sup>3</sup>College of Oceanic and Atmospheric Sciences, Oregon State University, Corvallis, OR 97331, USA.

\*To whom correspondence should be addressed. E-mail: preston@ess.washington.edu

## REPORTS

We interpret the reflector as the Moho of the subducting Juan de Fuca plate on the basis of two observations. First, the wide-angle reflections are often larger in amplitude than direct arrivals beyond 100-km source-receiver distance and are not observed closer than 55 km, indicative of postcritical reflections associated with an increase in velocities with depth across the reflector. Second, the 3D model demonstrates increases in velocities with depth in the vicinity of the reflector, leading to typical mantle velocities of 8 km/s just below the reflector.

We separate the intraslab earthquakes into two groups: those up-dip (west) of the 45-km reflector contour and those down-dip of this contour. The up-dip events generally occur at or below the reflector (Figs. 1 and 2). None of these events unambiguously occur above the reflector, considering the combined estimated 2-km uncertainty (14) in the earthquake locations and reflector position. In contrast, the down-dip events generally occur at or above the reflector, defining an 8-km-thick zone (Fig. 2).

We propose that the up-dip events occur within the subducted oceanic mantle. In the laboratory, serpentinite, a hydrated mantle rock expected to exist in the uppermost oceanic mantle (15), becomes brittle under dehydration conditions, forming a visibly wet, clearly defined fault in laboratory samples (16, 17). The pressure-temperature ( $P$ - $T$ ) conditions experimentally determined for this reaction coincide with the  $P$ - $T$  conditions predicted for Cascadia in the vicinity of the up-dip events (16, 18) (Fig. 3). Thus, we interpret the up-dip events as earthquakes induced by dehydration of serpentinite in the mantle. These mantle earthquakes are confined to a roughly 5-km-thick zone with a dip that is slightly shallower than that of the slab Moho, but which is parallel to predicted isotherms (18). Dehydration of serpentinite occurs nearly isothermally at these depths (Fig. 3), and thus this behavior is expected (19). In contrast, we propose that the down-dip events generally occur in the subducted oceanic crust as a result of embrittlement associated with progressive dehydration (Fig. 3).

The velocity of the rocks within which the earthquakes occur is consistent with this proposed spatial change in earthquake driving mechanism. The up-dip events nucleate in rocks with a velocity of 7.5 to 8.1 km/s, whereas the down-dip events nucleate in rocks with a velocity of 6.8 to 7.5 km/s (20). Deserpentinization of partially serpentinitized mantle rocks should result in an upper-mantle velocity of  $\sim$ 8 km/s, whereas eclogitization of lower oceanic crust should result in a progressive velocity increase from  $\sim$ 6.8 to 8 km/s (19).

Our interpretation requires knowledge of the relative locations of hypocenters, the re-

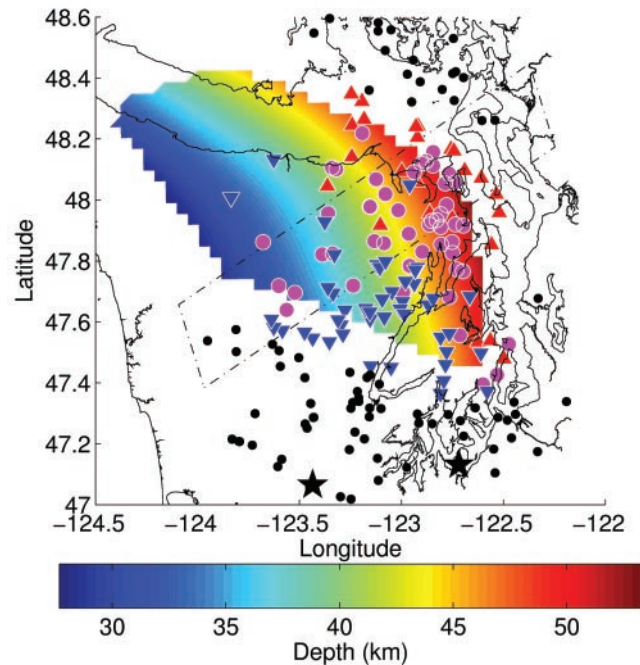


**Fig. 1.** Depth of reflector surface (colored area) and relocated intraslab earthquakes relative to the reflector [inverted blue triangles: more than 2 km beneath the reflector; maroon circles: within 2 km of the reflector; red triangles: more than 2 km above the reflector; black circles: reflector depth unknown; stars:  $M_w$  5.8 Satsop (left) and  $M_w$  6.8 Nisqually (right) earthquakes]. The dashed box corresponds to the cross section shown in Fig. 2 and is parallel to the relative plate motion direction.

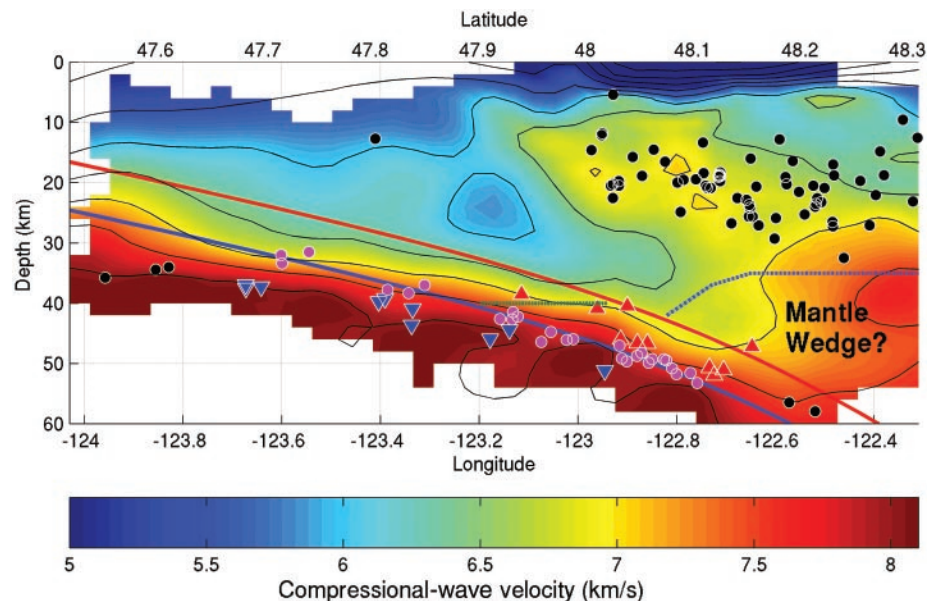
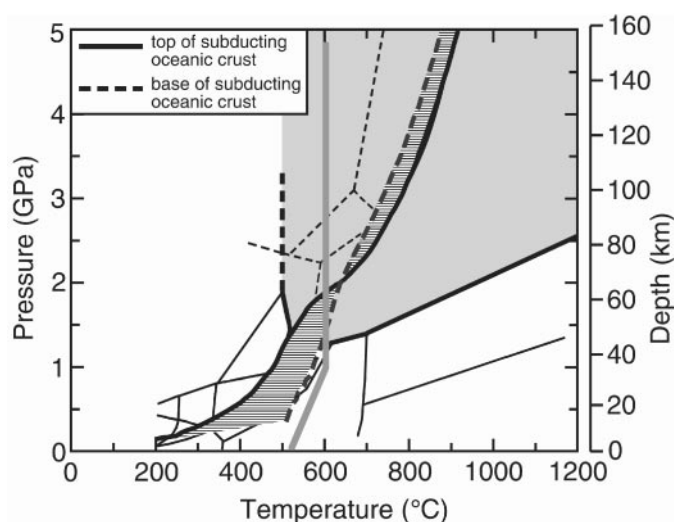


**Fig. 2.** Interpreted cross section (see dashed box in Fig. 1) showing compressional velocities (contoured at 0.5-km/s intervals), relocated seismicity (black circles: continental crustal events; colored symbols: intraslab events coded as described in Fig. 1), and Moho reflector (blue line). Interpreted top of subducting plate (red line) is drawn 7 km above reflector. The region between these lines is interpreted to be the subducting oceanic crust, composed of basalt above 40-km depth (horizontal green line) and beginning to transform to eclogite below. Subducting mantle is below the blue line. Low velocities in the mantle wedge imply the presence of serpentinite. There is no vertical exaggeration.

flector, and wave-speed contours to within about 2 km. We have performed specific resolution and error-analysis tests to determine our ability to resolve these parameters. Velocity checkerboard tests indicate the necessary resolvability, i.e., little smearing, strong pattern matching, and more than 50% amplitude return along the cross section shown in Fig. 2 using 30-km horizontal and

15-km vertical length scales, especially in the top 20 km of the model, but also within the subducting slab where earthquakes occur (fig. S2). To test whether we would be able to see a low-velocity zone (LVZ) associated with the subducted crust, we perturbed our model by placing an 8-km-thick LVZ above and parallel to the reflector, calculated travel times for this model, added random noise to

**Fig. 3.** Simplified phase diagram for the basalt (white)-to-eclogite (gray) transformation and serpentinite dehydration reaction (gray line) (19) overlaid with the calculated pressure-temperature path for the Cascadia slab (hashed). Note that, in the vicinity of the Cascadia geotherm, the basalt-to-eclogite transformation occurs at nearly constant pressure, independent of temperature, whereas the serpentinite dehydration reaction occurs at nearly constant temperature, independent of pressure. A geotherm just below the Moho would lie to the right (hotter) of the dashed line and, thus, would intersect the serpentinite dehydration line at a shallower depth. [Modified from (18)]



these times, and then inverted them (fig. S3). The inverted model shows only slight smearing of structure and demonstrates returns of more than 50% perturbed velocity amplitude throughout the region with earthquakes, and upward of 75% within the seismic region. Thus, we have the ability to resolve the velocity structure within the slab and at depths shallower than 50 km, and can state that the subducted crust is not a low-velocity wave guide.

In warm subduction zones, such as Cascadia and southwest Japan, circumstantial evidence has pointed to intraslab earthquakes occurring generally within the crust. Warm subduction zones lack the lower plane of intraslab seismicity, which is predominant in cold zones where it is clearly occurring within the subducting mantle. Thermal modeling showed that the seismicity cut-off of intraslab seismicity in southwest Japan (65 km) and in the cold subduction zone of northeast Japan (160 km) is consistent with the respective depths at which dehydration of the oceanic crust should be complete (21). However, intraslab seismicity in southwest and northeast Japan occur at much shallower depths than would be predicted for the basalt-to-eclogite transformation and indicate that basalt-to-eclogite reactions cannot explain all the seismicity. In Cascadia, which has a thermal structure similar to that of southwest Japan, the bulk of intraslab seismicity deeper than ~50 km was interpreted to occur within the subducting oceanic crust under southwest British Columbia (22). Farther to the south, under southwestern Washington, however, the bulk of intraslab seismicity (generally shallower than 40 km) was interpreted as occurring within the subducted mantle (8). Our results reconcile these apparently contradictory observa-

tions in Cascadia: The down-dip events occur within the subducted oceanic crust, and up-dip events occur primarily in the subducted oceanic mantle.

If intraslab earthquakes were purely caused by the basalt-to-eclogite transformation in the oceanic crust, the intraslab seismicity would be confined to the subducting crust. This geometrically constrains the maximum expected magnitude of an event to about  $M_w$  7 (23). Indeed, the three largest historical intraslab events in 1949, 1965, and 2001 are near this limit. Although we do not observe reflections in the vicinity of these events and, thus, are uncertain whether these events occur within the oceanic crust or mantle, the wave speeds are well constrained, suggesting that these events nucleate near the slab Moho. In Cascadia, earthquakes occur within the oceanic crust and mantle (Fig. 2), geometrically allowing the possibility of a larger event, such as the 2001  $M_w$  7.7 El Salvador intraslab earthquake.

Fluids released from the down-going plate by the basalt-to-eclogite or other transformations can have additional consequences. Slow slip events producing 2 cm of thrust-type slip may propagate a few hundred km along strike over a period of a few weeks (24, 25). These faults appear to coincide with the plate interface and extend down from the down-dip edge of the megathrust locked zone. Coincident in both space and time are recently discovered deep tremor events: nonimpulsive sources that are detected at 2 to 6 Hz (26) and may be caused by a fluid-driven process (27). Seven episodic slip events, with a repeat time of about 14 months, have been detected from the Olympic Mountains into southern or central Vancouver Island. The collocation of these deep-creep events with the region interpreted in our model to be undergoing trans-

formation of basalt to eclogite corroborates the hypothesis that these events are controlled by fluid processes. Geophysical evidence suggests the existence of a serpentinized continental mantle wedge in Cascadia (28). This would be expected because fluids released from the subducting plate infiltrate the overlying continental mantle. The lack of a well-defined continental reflector west of the Cascades is consistent with a serpentinized low-velocity mantle wedge. Indeed, wave speeds in our model at depths of 35 to 45 km in the mantle wedge are less than 7 km/s (Fig. 2), consistent with high concentrations of serpentinite.

#### References and Notes

- G. L. Choy, J. L. Boatwright, S. Kirby, *The Radiated Seismic Energy and Apparent Stress of Interplate and Intraslab Earthquakes at Subduction Zone Environments: Implications for Seismic Hazard Estimation* (U.S. Geol. Surv. Open-File Rep. 01-0005, 2001).
- S. H. Kirby, *J. Geophys. Res.* **92**, 13789 (1987).
- H. Houston, H. Green II, *Annu. Rev. Earth Planet. Sci.* **23**, 169 (1995).
- T. M. Brocher et al., *Wide-Angle Seismic Recordings from the 1998 Seismic Hazards Investigation in Puget Sound (SHIPS), Western Washington and British Columbia* (U.S. Geol. Surv. Open-File Rep. 99-314, 1999). The SHIPS experiment consisted of nearly 50,000 airgun sources within the inland waterways of northwest Washington and southwest British Columbia to more than 200 land-based stations.
- A. M. Trehu et al., in *The Cascadia Subduction Zone and Related Subduction Systems—Seismic Structure, Intraslab Earthquakes and Processes, and Earthquake Hazards*, S. Kirby, K. Wang, S. Dunlop, Eds. [U.S. Geol. Surv. Open-File Rep. 02-328 and Geol. Surv. Canada Open File 4350 (2002)], pp. 25–32.
- R. S. Ludwin, C. S. Weaver, R. S. Crosson, in *Neotectonics of North America*, D. B. Slemmons, E. R. Engdahl, M. D. Zoback, D. D. Blackwell, Eds. (Geological Society of America, Boulder, CO, 1991), Decade Map vol. 1, pp. 77–97.
- T. M. van Wagoner et al., *J. Geophys. Res.* **107**, 2381, 10.1029/2001JB000710 (2002).
- T. Parsons et al., *Geology* **26**, 199 (1998).
- The magnitude range for 95% of these events is between 2.5 and 4.0; however, our data set includes a few events with larger magnitudes, up to 6.8.
- L. A. Preston, thesis, University of Washington, Seattle (2003).
- J. Vidale, *Geophysics* **55**, 521 (1990).
- J. Hole, B. Zelt, *Geophys. J. Int.* **121** (1995).
- R. Crosson, *J. Geophys. Res.* **81**, 3047 (1976).
- Materials and methods are available as supporting material on Science Online.
- B. R. Hacker, G. A. Abers, S. M. Peacock, in *The Cascadia Subduction Zone and Related Subduction Systems—Seismic Structure, Intraslab Earthquakes and Processes, and Earthquake Hazards*, S. Kirby, K. Wang, S. Dunlop, Eds. [U.S. Geol. Surv. Open-File Rep. 02-328 and Geol. Surv. Canada Open File 4350 (2002)], pp. 123–137.
- C. Raleigh, M. Paterson, *J. Geophys. Res.* **70**, 3965 (1965).
- E. H. Rutter, K. Brodie, *J. Geophys. Res.* **93**, 4907 (1988).
- S. M. Peacock, K. Wang, A. M. McMahon, in *The Cascadia Subduction Zone and Related Subduction Systems—Seismic Structure, Intraslab Earthquakes and Processes, and Earthquake Hazards*, S. Kirby, K. Wang, S. Dunlop, Eds. [U.S. Geol. Surv. Open-File Rep. 02-328 and Geol. Surv. Canada Open File 4350 (2002)], pp. 123–126.
- B. R. Hacker, G. A. Abers, S. M. Peacock, *J. Geophys. Res.* **108**, 2029, 10.1029/2001JB001127 (2003).
- The mean and standard deviations of the compressional-wave velocities at the intraslab earthquake locations, grouped according to the event depth relative to the reflector, are as follows:  $7.3 \pm 0.3$  km/s for events more than 2 km above the reflector;  $7.6 \pm$

0.3 km/s for events within 2 km; and  $7.9 \pm 0.1$  km/s for events more than 2 km below the reflector. See table S1 for distribution.

21. B. R. Hacker, S. M. Peacock, G. A. Abers, *J. Geophys. Res.* **108**, 2030, 10.1029/2001JB001129 (2003).

22. J. F. Cassidy, R. M. Ellis, *J. Geophys. Res.* **98**, 4407 (1993).

23. For example, fault width =  $2 \times$  crustal thickness = 15 km for a fault plane subparallel to slab dip, twice as long as is wide = 30 km, having 1.5-m slip, rigidity of basalt =  $5 \times 10^{10}$  Pa gives,  $M_0 =$  rigidity  $\times$  width  $\times$  length  $\times$  slip =  $3 \times 10^{19}$  N-m,  $M_w = (2/3)\log(M_0) - 6.06 = 7.0$ .

24. H. Dragert, K. Wang, T. S. James, *Science* **292**, 1525 (2001).

25. M. M. Miller, T. Melbourne, D. J. Johnson, W. Q. Sumner, *Science* **295**, 2423 (2002).

26. G. Rogers, H. Dragert, *Science* **300**, 1942 (2003).

27. K. Obara, *Science* **296**, 1679 (2002).

28. T. M. Brocher, T. Parsons, A. M. Trehu, C. M. Snelson, M. A. Fisher, *Geology* **31**, 267 (2003).

29. This study was supported by the U.S. Geological Survey and by the NSF. We thank the SHIPS Working Group (M. A. Fischer, T. Parsons, R. A. Hyndman, K. C. Miller, C. N. Snelson, D. C. Mosher, T. L. Pratt, R. Ramachandran, G. D. Spence, U. S. ten Brink, C. S. Weaver, and B. C. Zelt) for providing data and contributing to the success of the experiment, and for advice and discussions. We also thank N. P.

Symmons for help with the tomography code; G. Medema, T. M. Van Wagoner, and Qing Xu for helpful discussions; and B. Hacker, R. Blakely, and P. McCrory for reviews.

**Supporting Online Material**  
www.sciencemag.org/cgi/content/full/302/5648/1197/DC1

Materials and Methods  
Figs. S1 to S5  
Table S1  
References

25 August 2003; accepted 15 October 2003

## Detection of a Human Influence on North American Climate

David J. Karoly,<sup>1\*</sup> Karl Braganza,<sup>2</sup> Peter A. Stott,<sup>3</sup> Julie M. Arblaster,<sup>4</sup> Gerald A. Meehl,<sup>4</sup> Anthony J. Broccoli,<sup>5†</sup> Keith W. Dixon<sup>5</sup>

Several indices of large-scale patterns of surface temperature variation were used to investigate climate change in North America over the 20th century. The observed variability of these indices was simulated well by a number of climate models. Comparison of index trends in observations and model simulations shows that North American temperature changes from 1950 to 1999 were unlikely to be due to natural climate variation alone. Observed trends over this period are consistent with simulations that include anthropogenic forcing from increasing atmospheric greenhouse gases and sulfate aerosols. However, most of the observed warming from 1900 to 1949 was likely due to natural climate variation.

Most of the observed global-scale warming over the last 50 years is believed to have been due to the increase in atmospheric greenhouse gas concentrations (1). Here, we investigated the causes of climate change in the North American region over the 20th century with the use of a number of simple indices of large-scale surface temperature variation. These indices represent different aspects of both natural climate variability and the expected climate response to increasing greenhouse gases (2). Previous studies of the possible causes of 20th-century climate change have concentrated on global-scale patterns of temperature change (3). The magnitude of any greenhouse gas-induced climate change signal relative to natural climate variability decreases as the spatial scale of consideration is reduced (4). This explains the focus of most climate change detection and attribution

studies on global scales. Recently, it has been shown that an anthropogenic climate change signal may be detectable in the North American region by analysis of surface temperature changes over the past 50 years (5, 6).

Significant changes in North American temperatures occurred during the second half of the 20th century (1, 7). We investigated the causes of these changes by comparing observed temperature changes during the 20th century to simulations performed with five different climate models. The simulations represent the natural internal variability of climate as well as its response to human influences, such as increases in atmospheric greenhouse gases and sulfate aerosols. Natural external influences (changes in solar irradiance and volcanic aerosols) are also included. We sought to identify whether there has been a significant human influence on observed surface temperature changes in the North American region over the 20th century.

We used a small number of indices of area-average surface temperature variation (2). These were chosen to represent different aspects of climate variation in the North American region, defined here as a rectangular region (30° to 65°N, 40° to 165°W) encompassing the United States and Canada and the surrounding ocean region. The simple indices are as follows: NA, North American area-mean surface air temperature over land;

LO, mean land-ocean temperature contrast (area-mean temperature over land minus the mean sea surface temperature for the surrounding region); MTG, meridional temperature gradient in the North American region [mean temperature over land in higher latitudes (Canada, 50° to 70°N) minus that in middle latitudes (United States, 30° to 50°N)]; AC, mean magnitude of the annual cycle in temperature over land [area-mean temperature in summer (June–August) minus that in winter (December–February)]; and DTR, mean diurnal temperature range over land (area-mean daily maximum temperature minus minimum temperature).

The indices represent the main features of the modeled surface temperature response to increasing greenhouse gases, such as faster warming over land than over ocean, faster warming in winter than in summer, faster warming of nighttime minima than of daytime maxima, and faster warming at higher latitudes. Because the indices (apart from NA) are defined as differences, they are likely to contain information independent of that in NA. In addition, defining indices on the basis of large area averages significantly enhances the signal-to-noise ratio, increasing the likelihood of climate change detection (5).

Observed seasonal-mean gridded surface temperature data for the period 1881 to 1999 (8) were used to calculate the indices. These data were obtained from quality-controlled instrumental observations and have been used in virtually all detection studies considering surface temperature changes. Observed diurnal temperature range data were obtained from a different data set (9). Annual means were constructed using seasonal averages from December of the previous year to November. Because high-latitude areas have fewer data available for the early part of the 20th century, we stipulated that only regions with data available throughout most of the 20th century were considered in the analysis. This yields a time-invariant data “mask,” which was applied to both the observations and climate model output before the calculation of the indices. The time series of annual means were low-pass filtered (10) to estimate variability on decadal time scales.

<sup>1</sup>School of Meteorology, University of Oklahoma, Norman, OK 73019, USA. <sup>2</sup>School of Mathematical Sciences, Monash University, Clayton, Victoria 3800, Australia. <sup>3</sup>Hadley Centre, MetOffice, Bracknell RG12 2SY, UK. <sup>4</sup>National Center for Atmospheric Research (NCAR), Boulder, CO 80307, USA. <sup>5</sup>Geophysical Fluid Dynamics Laboratory, National Oceanic and Atmospheric Administration, Princeton, NJ 08542, USA.

\*To whom correspondence should be addressed. E-mail: dkaroly@ou.edu

†Present address: Department of Environmental Sciences, Rutgers University, New Brunswick, NJ 08901, USA.

## Supplemental Online Material:

**Material and Methods:** We performed several parameter sensitivity tests to investigate the robustness of the locations of the intraslab hypocenters relative to the reflector. For example, we moved all the intraslab earthquakes in depth, fixed their depths, and inverted keeping all other parameters free as they were in the original inversion. We then compared the resulting intraslab earthquake and reflector travel-time residual variances to those of the best model. We performed these tests for the intraslab earthquake depths moved by -5,-2,+2, and +5 km and for the reflector depth moved by -5,-2,+2, and +5 km (Figs. S4 and S5). These tests indicate that we can resolve the relative locations of the reflector and intraslab events to within 2km, though the uncertainty of individual events can be larger (*l*).

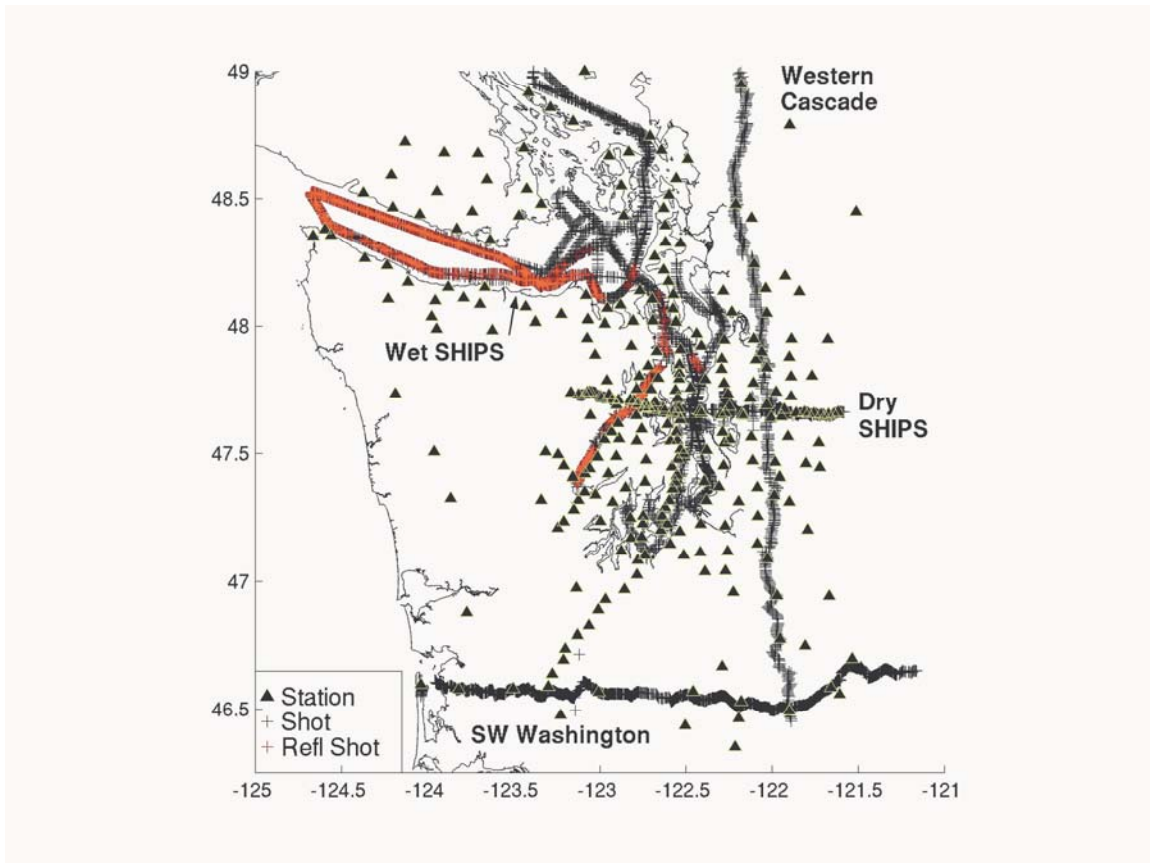


**Figure S1:** Source-Receiver geometry for fixed sources (black +), receivers (triangles), and wide-angle reflection sources (red +). The shot lines for the various experiments are labeled.

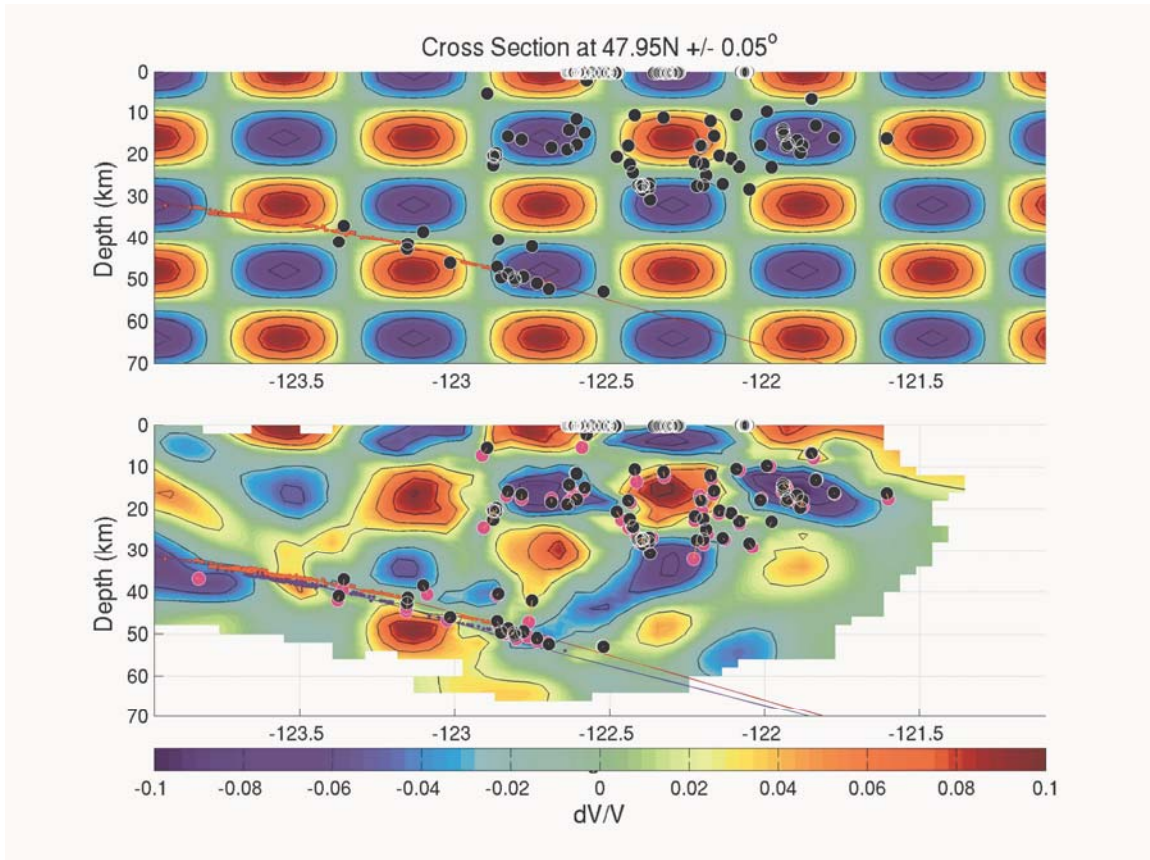


**Figure S2:** Velocity model resolution test. Input model (top) is displayed as perturbations to the final model given by sine waves in all 3 dimensions, and retrieved model (bottom) with input hypocenter positions (black) and retrieved hypocenters (magenta) connected by a thin yellow line, input reflector (red) and retrieved reflector (blue). Contours are at 0.025  $dV/V$  intervals, excluding 0.0.

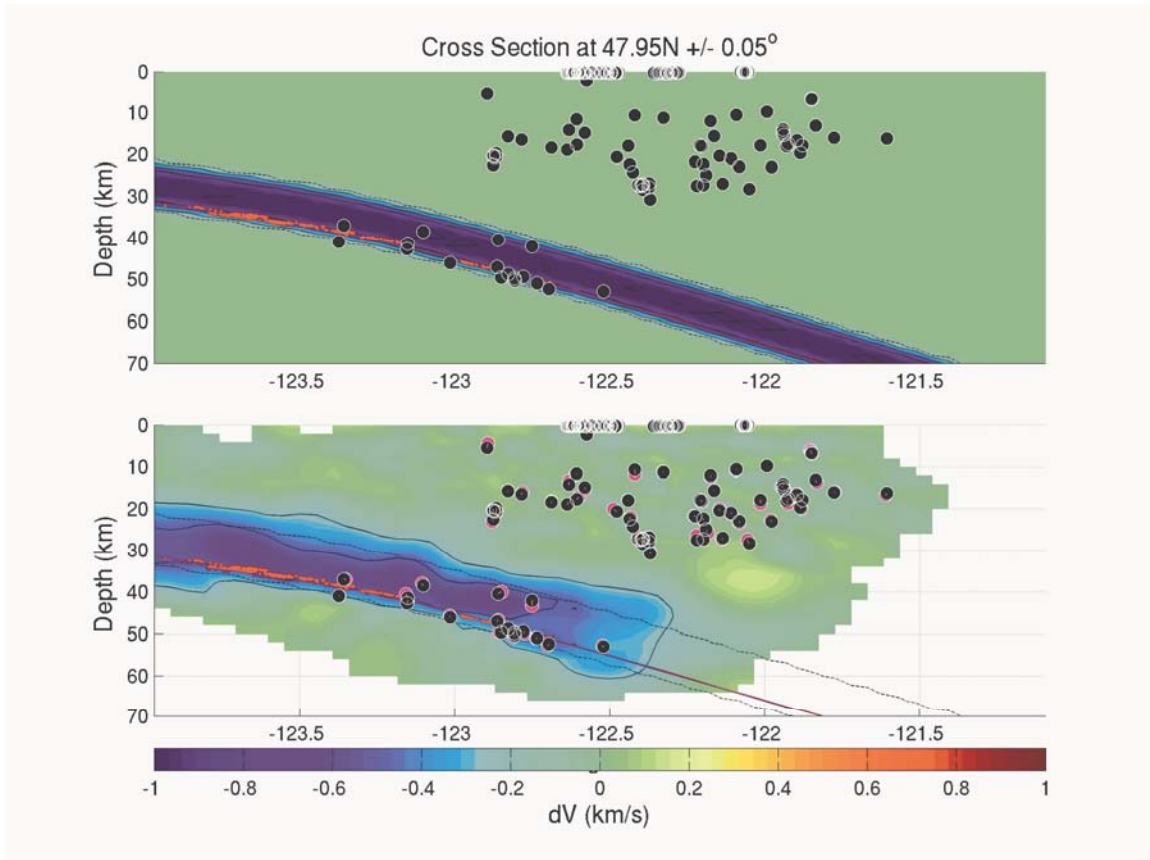


**Figure S3:** Slab velocity resolution above the reflector. Imposed perturbation to the velocity model (top) and retrieved (bottom). Contours are at 0.25 km/s increments starting at  $-0.25$  km/s. The dashed lines in both panels enclose the perturbation envelope in the input model. Black circles, red line and red dots are input hypocenters, reflector and bounce points respectively. Magenta circles, blue line and blue dots are retrieved hypocenters, reflector and bounce points.

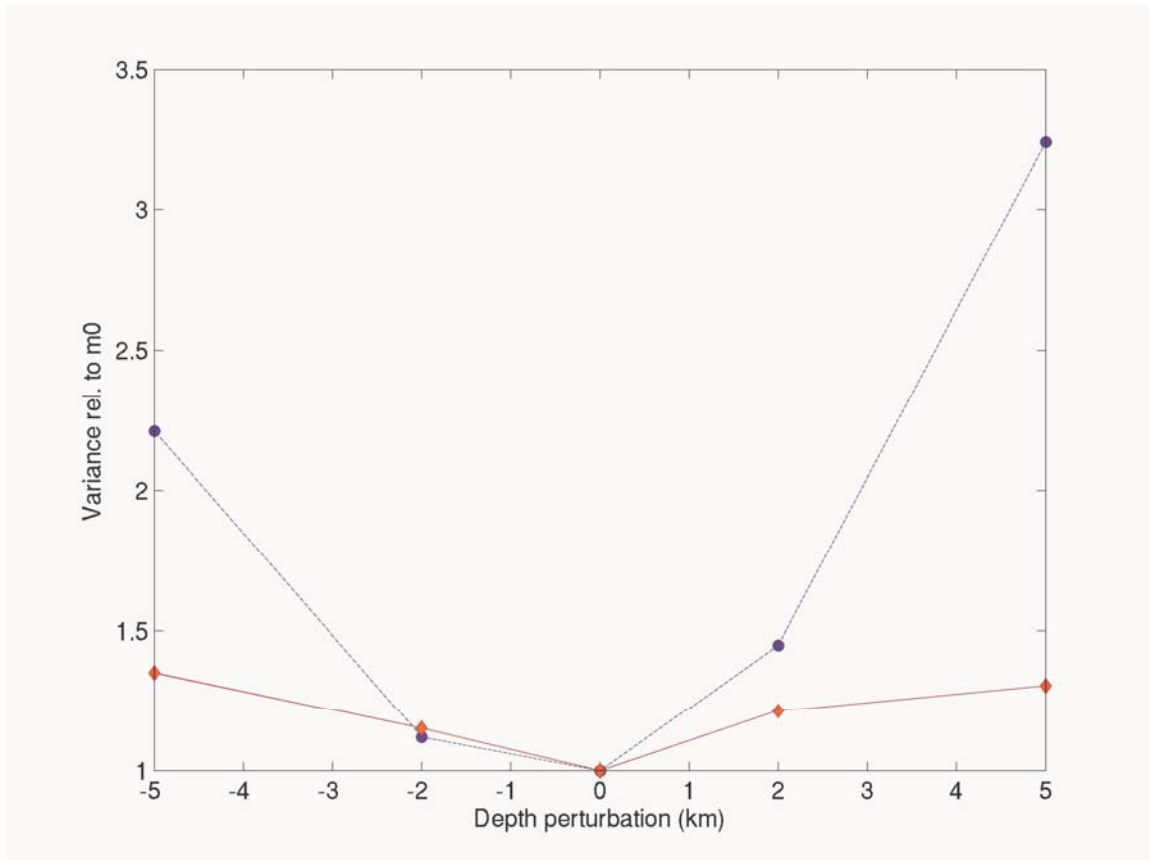


**Figure S4:** Ratios of travel-time residual variances relative to the best model for the reflection times in the cases where the reflector is displaced (dashed line) and for the intraslab earthquake times in the cases where the intraslab hypocentral depths are displaced (solid line). Fixed depth displacements relative to best model are shown along the horizontal axis. Standard F-tests indicate that a 5% increase in variance for the earthquake data and a 10% increase in variance for the reflection data are statistically significant at the 95% confidence level; however, F-tests assume statistical independence of the data, which is clearly not the case. Thus, we conservatively assume that a 20% increase in variance represents a statistically significant difference, and conclude that the intraslab earthquakes can move up to 2 km both deeper and shallower and that the reflector can move about 2 km shallower but only 1 km deeper.

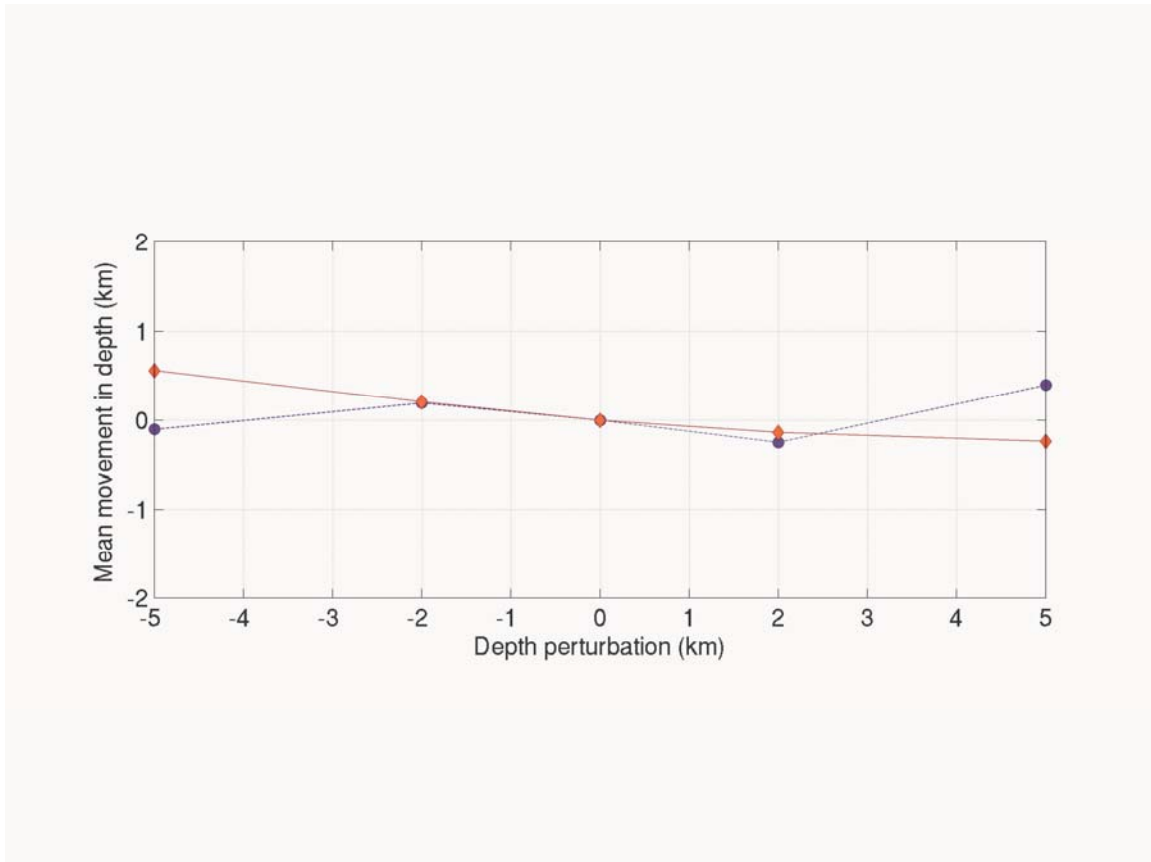


**Figure S5:** Variations in mean depth displacement relative to best model for the reflector in the fixed intraslab earthquake depth tests (dashed) and for the intraslab earthquakes in the fixed reflector depth tests (solid). The mean reflector depth only changes by a few hundred meters even when the intraslab earthquakes are moved 5 km from their best position. Likewise, the mean intraslab earthquake depth varies little when the reflector is forced to move. Thus, the two data sets are able to determine their respective average depths nearly independently of each other.

**Table S1:** Distribution of compressional-wave speeds at locations of each intraslab earthquake grouped according to the event depths relative to the reflector (see Fig. 1 for definition of groups).

$V_P$ (km/s)	> 2 km above	Within 2 km	> 2 km below
6.6-6.8	1	1	0
6.8-7.0	4	3	0
7.0-7.2	4	4	0

7.2-7.4	5	2	0
7.4-7.6	8	7	2
7.6-7.8	5	13	5
7.8-8.0	0	14	20
8.0-8.2	0	4	15

**Supporting References and Notes:**

1. L. A. Preston, Simultaneous Inversion of 3D Velocity Structure, Hypocenter Locations, and Reflector Geometry in Cascadia, Ph.D. thesis, University of Washington, Seattle (2003).